Enhancement of magnetic properties of Ni–Mg–Co ferrites by Y^{3+} ions doping

Lichao Yu[1] · Aimin Sun[1,2] · Nanzhaxi Suo[1] · Zhuo Zuo[1] · Xiqian Zhao[1] · Wei Zhang[1] · Liqionsg Shao[1] · Yanchun Zhang[1]

Abstract

In this study, yttrium ion-doped nickel–magnesium–cobalt ferrite powder was prepared by the sol–gel auto combustions method. The chemical formula is $Ni_{0.2}Mg_{0.1}Co_{0.7}Fe_{2-x}Y_xO_4$ (where $x = 0.00$, 0.02, 0.04, 0.06, and 0.08). The structure and magnetic properties were studied by X-ray diffractometer (XRD), Fourier infrared spectroscopy (FTIR), ultraviolet–visible (UV–Vis), scanning electron microscope (SEM), and vibrating sample magnetometer (VSM). XRD measurements show that Ni–Mg–Co ferrite has a good phase formations, and all samples have single-phase cubic spinel structure. As the doping amount of yttrium ions increases, the lattice constant of the samples increases first and then decreases. FTIR measurements also confirm the formations of the cubic spinel structure of ferrite. The UV–Vis optical analysis shows that the bandgap value of optical energy decreases after doping Y^{3+} ions. SEM confirmed that the sample was spherical spinel with a particle size of 54–60 nm. The saturation magnetizations (M_s) and remanent magnetizations (M_r) increase first and then decrease with the increase of Y^{3+} ions content at room temperature. This shows that the small amount of Y^{3+} ions-doped nickel–magnesium–cobalt nanoferrite can optimize the magnetic properties of the ferrite. The coercivity of the samples also showed a downward trend. The comprehensive measurement data show that the sample has the best magnetic properties when $x = 0.02$. This is also confirmed that the ferrite can be used as magnetic storage material.

1 Introduction

Ferrite, as the name suggests, is an oxide of iron, derived from magnetite containing Fe_3O_4 as the main component; in addition, Fe_2O_3 is also a common semiconductor material [1, 2]. This is the earliest non-metallic magnetic material used in the world [3]. Early ferrite was a complex oxide containing iron oxide and transitions elements. With the continuous development of ferrite materials, its composition may not contain iron oxide, so ferrite has become a special noun for nonmetallic magnetic materials. The ferrite generally referred to is a composite oxide of one or more metal elements mainly composed of iron. Most of the oxide found to have strong magnetic [4] properties and high curie points

contain iron ions, which is also the main reason for the name ferrite. Spinel ferrite has good electromagnetic properties, and it has been a research hotspot of functional materials due to its wide applications in informations storage systems, medical diagnostic technology, magnetic fluid technology, magnetocaloric heating, and refrigerations [5, 6]. Among the ferrite of the spinel structure, cobalt ferrite ($CoFe_2O_4$) has many unique physical properties and chemical properties. It has high saturations magnetizations, high magnetocrystalline anisotropy constant, high magnetostrictions coefficient, high resistivity and low eddy current loss, stable chemical properties, corrosions resistance, and wear resistance [7, 8]. It has been widely used. This is the main reason why ferrite is used in permanent magnets, magnetic measurement and magnetic induction, microwave equipment, high-density information storage and other applications [9]. The magnetic properties of cobalt ferrite materials are mainly affected by the following factors: chemical compositions, type and amount of doping ions, preparations conditions, sinter temperature, sinter time, and the like. In particular, ion doping has a great influence on the performance of ferrite [10]. From the crystal structure, the ferrimagnetic property

✉ Aimin Sun
sunam@nwnu.edu.cn

1 College of Physics and Electronic Engineering, Northwest Normal University, Lanzhou 730070, China

2 Key Laboratory of Atomic and Molecular Physics & Functional Materials of Gansu Province, Lanzhou 730070, China

of the cobalt ferrite [11] material is caused by the fact that the reverse arrangement of the magnetic ions magnetic moments at the A and B positions. Therefore, which metal ions occupy the A positions or which occupy the B positions are closely related to the magnetic properties. Many researchers have done a lot of work to study the effects of doping Li^+, Ti^{4+}, Ge^{4+}, Ga^{3+}, Cr^{3+}, Zn^{2+}, Mn^{3+}, and Al^{3+} on the structure and properties in $CoFe_2O_4$ [12, 13]. Rare earth substituted different ferrites are becoming promising materials for various applications. Addition of small amount of rare earth ions to ferrite sample alters their electrical, magnetic, and structural properties depending upon the type and amount of rare earth element used [14–16]. Looking up a large number of literature found that the research on cobalt ferrite has been very sufficient, and the research on doping cobalt ferrite is more perfect [17–19]. One of the papers is about the magnetic properties and microstructure of Ni–Mg–Co ferrite. After reading it, we found it very interesting. Therefore, we decided to mix rare earth ions into the Ni–Mg–Co ferrite system, so as to study the influence of different rare earth ions content on the magnetic properties and microstructure of Ni–Mg–Co ferrite. Based on the above, we decided to prepare yttrium-doped nickel–magnesium–cobalt nanoferrite and use X-ray diffractometer, Fourier transform infrared spectroscopy, vibrating sample magnetometer, transmission electron microscope, scanning electron microscope, and other instruments to characterize the sample. The structural morphology and the change in magnetic properties of the prepared samples were investigated.

This article used sol–gel self-propagating technology which can significantly save time and energy consumptions and requires a lower sintering temperature, compared to traditional methods. Sol–gel self-propagating technology to prepare ferrite, this method generally includes hydrolysis reactions, polycondensations reactions, gelations, aging process, drying, sintering these several processes. The formation of the precursor is mainly due to the existence of the first two chemical reactions: the hydrolysis reactions and the polycondensations reactions. The starting materials (precursors) used in the reactions are generally metal alkoxides, certain salts, hydroxides, or complexes. The main reaction step is that the precursor is dissolved in the solvent (water or organic solvent) to form a uniform solutions. The solute and the solvent produce a hydrolysis reactions or alcoholysis reactions. The reaction product aggregates into particles of about 1 nm and forms a sol, which is transformed into a gel by evaporations and drying. In additions, it also uses the redox exothermic reactions of nitrate and some organic fuels (such as citric acid, urea) to cause self-propagating combustions to obtain ferrite powder. The hydrolysis reactions refer to the hydrolysis reactions of a metal or semi-metal alkoxide precursor to form a hydroxylated product and the corresponding alcohol. The polycondensations reaction

refers to two types of polycondensations reactions: water loss polycondensations and alcohol loss polycondensations. Analysis of the sample characterizations results shows that the doping of yttrium ions will change the microstructure of ferrite and the magnetic properties of the sample. And with the increase of doping amount of yttrium ions, the magnetic properties of the sample showed the law of increasing first and then decreasing. This shows that the incorporations of trace rare earth ions can improve the magnetic properties of nickel–magnesium–cobalt ferrite.

2 Experimental process

The yttrium ions-doped nickel–magnesium–cobalt ferrites powder was prepared by the sol–gel natural sintered method. The detailed process of preparations is shown in Fig. 1, and its chemical formula was $Ni_{0.2}Mg_{0.1}Co_{0.7}Fe_{2-x}Y_xO_4$ ($x = 0.00$, 0.02, 0.04, 0.06 and 0.08). The chemicals used were analytically pure nickel nitrate $Ni(NO_3)_2 \cdot 6H_2O$, magnesium nitrate $Mg(NO_3)_2 \cdot 6H_2O$, cobalt nitrate $Co(NO_3)_2 \cdot 6H_2O$, ferric nitrate $Fe(NO_3)_3 \cdot 9H_2O$, yttrium nitrate $Y(NO_3)_3 \cdot 3H_2O$, and citric acid $(C_6H_8O_7 \cdot H_2O)$. The specific step is (1) to dissolve the stoichiometric metal nitrate together in an appropriate amount of deionized water; (2) the amount of the substance added with citric acid should be 1.2 times that of the metal cations. Add an appropriate amount of ammonia water to the solutions to adjust the pH of the solutions so that the pH of the solutions = 7; (3) after the magnetic stirrer was adjusted to a constant temperature of 80 °C and the rotation speed was 300 rpm, the solution was heated in a water bath and stirred at a uniform speed until a wet gel was formed; (4) the formed gel was then dried in a drying box for 2 h; (5) the dried sample was taken out and ignited to obtain a silver-gray powder, which was then ground for 45 min, placed in a tube furnace, and sintered at 950 °C for 3 h under non-vacuum conditions; and (6) Ground in agate for 15 min to obtain a final product.

3 Results and discussions

3.1 Structural characterizations

An X-ray diffractometer (XRD) was used to characterize the sample, and the image obtained is shown in Fig. 2. The main peak (311) and characteristic peaks (111), (220), (222), (400), (422), (511), and (440) can be clearly seen in the figure. The above diffractions peaks all correspond to the spinel structure, which indicates that the proper introductions of yttrium ions in the ferrite can replace the iron ions on the octahedral positions, but the ferrite still strictly conforms to Bragg's law. Detailed analysis of the image shows that the
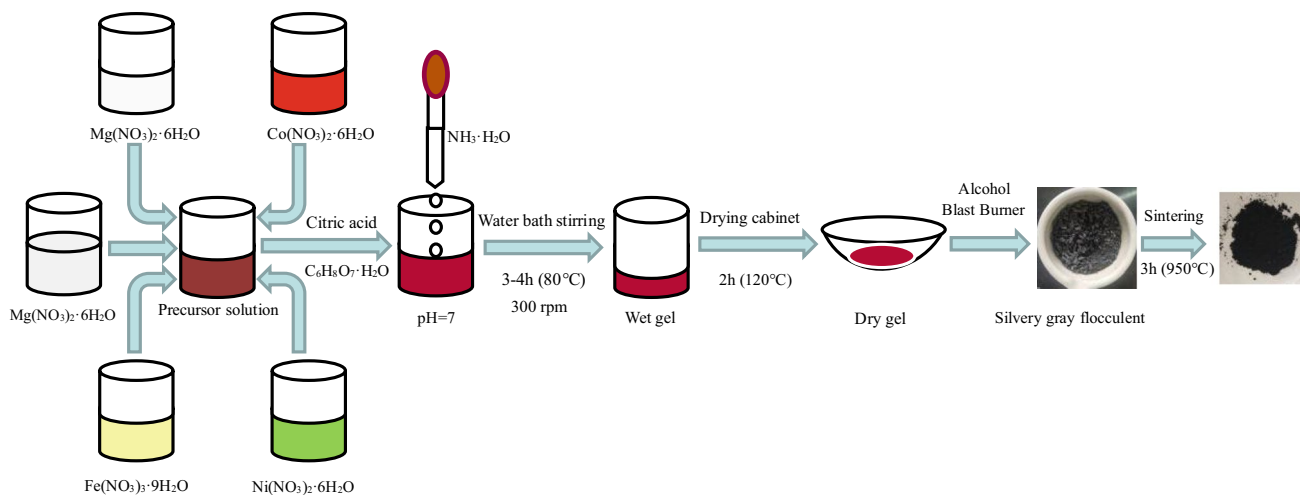
Fig. 1 Flow chart for the synthesis of $Ni_{0.2}Mg_{0.1}Co_{0.7}Fe_{2-x}Y_xO_4$ nanoferrite particles by sol–gel auto combustion process
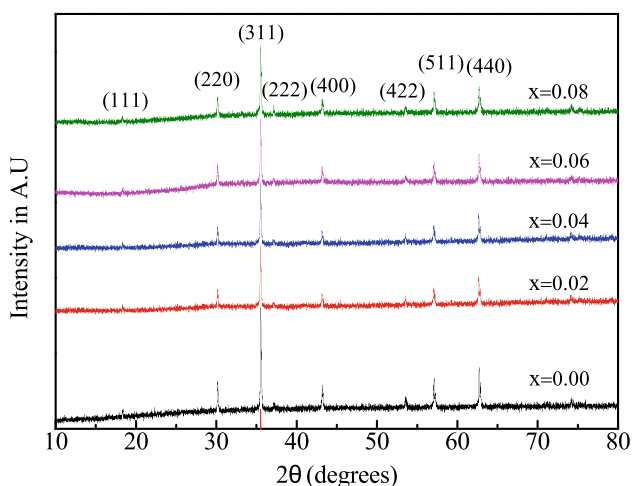
Fig. 2 The XRD pattern of $Ni_{0.2}Mg_{0.1}Co_{0.7}Fe_{2-x}Y_xO_4$ ($x=0.0, 0.02, 0.04, 0.06, 0.08$) nanoferrites along with the figure showing the shifting of the most intense (311) peak

prepared samples have spinel structure with good crystallinity, and no impurity peaks are found in the whole X-ray diffractions pattern [20, 21]. Therefore, the sample had a ferrites pure phase structure. The peak of the measured image was compared with the JCPDS (No. 22-1086) phase standard card [22]. Therefore, the prepared samples and $CoFe_2O_4$ belong to the same structure, i.e., they are spinel structure.

Further analysis of Fig. 2 shows that as the amount of yttrium ions incorporated into the nickel–magnesium–cobalt ferrites increases, the (311) diffraction peak of the sample shifts to a small angle. This is mainly because the radius of the yttrium ions is larger than the radius of the iron ions. When the yttrium ions enter the crystal lattice, the crystal lattice expands and the interplanar spacing

increases, so the diffraction peak shifts to a low angle. In addition, theoretically a part of the Y^{3+} ions replaces part of the Fe^{3+} ions in the nickel magnesium cobalt ferrite, and another part of the Y^{3+} ions may reside in the grain boundary in the form of an oxide. However, there is no significant phase of yttrium oxide in the XRD pattern. This may be due to the low resolutions of the instrument or the large step size resulting in a less pronounced phase of yttrium oxide.

Process the XRD spectrum in jade6.5 to obtain the interplanar distance (d) of the sample and other parameters describing the microstructure of the sample. The following formula is used to calculate the parameters such as inter lattice constant (a), average crystallite size (D), cell volume (a^3), and dislocations linear density (δ), which are shown in Table 1.

The lattice constant is obtained by the following formula [23, 24]:

$$a = d\sqrt{h^2 + k^2 + l^2} \tag{1}$$

Here, d is the interplanar spacing corresponding to the (311) peak of the X-ray diffractions, 'h', 'k', and 'l' are their Miller indices, and a is the lattice constant. From the table, we find that the lattice constant of ferrite after Y^{3+} doping increases. The theoretical density obtained by X-ray diffractions is calculated according to the following formula [25]:

$$\rho_x = \frac{8M}{N_A a^3} \tag{2}$$

In the formula, 'M' is the molecular mass of the sample, 'N_A' is the Avogadro constant (6.02×10^{23}), and 'a' is the lattice constant. The appropriate amount of the prepared sample powder was pressed into a sheet at 11 MPa using a

Table 1 Parameters obtained from XRD data for $Ni_{0.2}Mg_{0.1}Co_{0.7}Fe_{2-x}Y_xO_4$ nanoferrite particles

Composition, x	Inter planar spacing 'd' (Å)	Lattice constant 'a' (Å)	Grain size 'D' (nm)	Volume of unit cell 'a^3' (Å^3)	Dislocation line density 'δ' (10^{-4} nm^{-2})
0.00	2.5227	8.3668	60.89	585.7	2.70
0.02	2.5240	8.3711	50.87	586.6	3.87
0.04	2.5245	8.3728	49.95	586.9	4.01
0.06	2.5239	8.3708	52.46	586.5	3.63
0.08	2.5238	8.3704	54.52	586.4	3.36

tableting machine, and the block density was calculated by the following formula [26]:

$$\rho_b = \frac{M_s}{\pi R^2 t} \tag{3}$$

Here. 'M_s' is the mass of the tablet, 't' is the thickness of the tablet, and 'R' is the radius of the tablet. The grain size of the sample can be calculated using the Scherrer formula [27]:

$$D = \frac{0.9\lambda}{\beta \cos\theta} \tag{4}$$

In the formula, 'D' is the average size of the crystal grains perpendicular to the crystal plane directions, 'β' is the full-width at half-maximum (FWHM) of the (311) diffractions peak, and 'θ' is the diffractions angle, which 'λ' is the X-ray wavelength (1.5406 Å).

The dislocation line density of the prepared sample was calculated by the following formula [28]:

$$\delta = \frac{1}{D^2} \tag{5}$$

The porosity 'P' of samples was deduced from bulk 'ρ_b' and X-ray densities 'ρ_x' using the formula:

$$\text{Porosity } P\ (\%) = \frac{\rho_x - \rho_b}{\rho_x} \times 100 \tag{6}$$

Figure 3a is a change graph of the lattice constant and grain size of the sample as a function of yttrium ion content. It can be seen from Fig. 3a that the nanoferrite grain size decreases first then increase as the doping amount of yttrium ions increases the lattice constant first increases and then decreases. The lattice constant increases with the amount of yttrium ions doping, which happens because the yttrium ions radius (0.9 Å) is much larger than the Fe^{3+} ions radius (0.64 Å). The rule of ion substitutions is that the substituted ions have similar ionic radii and valence states, while the tetrahedral A positions gap is smaller than the octahedral B positions gap, so the possibility of yttrium ions entering the tetrahedral A positions is excluded and it can only enter the B positions of the octahedron, so the yttrium ions enter the B site of the spinel ferrite to replace the Fe^{3+} ions.

Since the Y^{3+} (0.95 Å) radius is greater than the Fe^{3+} (0.67 Å) radius, the lattice expands and the lattice constant a becomes larger. With the increase of doping amount of yttrium ions, the grain size of nickel–magnesium–cobalt ferrite decreases, which is mainly caused by the following two reasons: (1) the radius of the Y^{3+} ions is much larger than the Fe^{3+} ions radius, and the bond energy of the Y–O bond is greater than the bond energy of the Fe–O bond, so more energy is needed to get the Y^{3+} ions into the lattice to form the Y–O bond. All samples doped with Y^{3+} ions have higher thermal stability than pure nickel–magnesium–cobalt ferrite, so the doped samples require higher energy for
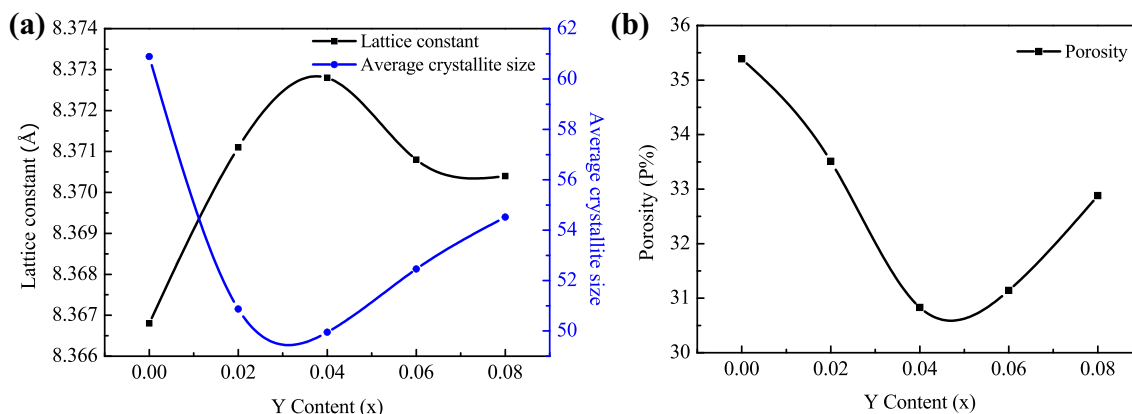

Fig. 3 Variation of lattice constant, average crystallite size, and porosity versus of Y content (x)

crystallizations and grain growth. (2) A part of the Y^{3+} ions replaces part of the Fe^{3+} ions in the nickel magnesium cobalt ferrite, and another part of the Y^{3+} ions may reside in the grain boundary in the form of an oxide. Oxide appears in the grain boundary to exert a certain pressure on the internal grain size, thereby hindering the growth of the crystal grains. Therefore, the larger the doping amount, the higher the barrier of the rare earth ions entering the spinel B positions. And it causes a certain degree of lattice distortions. The decrease of lattice constant is mainly due to the formations of a small amount of metal oxides at the grain boundary, so that the external stress is greater than the internal stress and the lattice constant decreases. It can also be seen in Table 1 that the average size tends to decrease first and then increase with the increase of the doping amount of Y^{3+} ions. In the prepared sample, the grain size of the sample was the smallest when $x = 0.04$. As the doping concentrations is further increased, more and more iron ions are replaced by yttrium ions, and the positive charge around the particles will begin to increase causing a charge imbalance. In order to eliminate this imbalance, the exchange rate between ions will increase, which promotes the growth of ferrite grains and thus increases the grain size.

It can also be seen in Table 1 that as the amount of doping change, the grain size becomes smaller and the dislocation density becomes first to grow bigger and then smaller. Since the radius of the Y^{3+} ions doped into the crystal lattice is large, the hop length of the sample is increased. In addition, the lattice constant of the sample changes. From the calculation formula, the dislocations' linear density, and jump length of the sample will change correspondingly with the lattice constant (Table 2).

In addition, as shown in Fig. 3b, the porosity of the sample is first decreased and then increased. This may be because the solid particles come into contact with each other at the initial stage of sintering, and the pores are dispersed and penetrated each other. With the volatilizations of moisture and other impurities, the pores escape through the surface of the pellet. Porosity decreases, shrinkage increases, and body density increases slightly. In the middle of sintering, as the temperature increases, the interfaces of individual solid pellets gradually merge, and the interpenetrating pores

are gradually closed and relatively concentrated. Porosity decreases rapidly. Shrinkage increases significantly, body density decreases. In the later stage of sintering, with the further increase of temperature, the number of closed pores decreased, the bulk density increased significantly, and the density identified and tended to be perfect However, if the sintering temperature is too high, the partial decompositions of Fe_2O_3 will occur, which will lead to the increase of porosity and decrease of shrinkage.

3.2 Cations distributions in ferrite

For $[Fe^{3+}_{0.1}][Ni^{2+}_{0.2}Mg^{2+}_{0.1}Co^{2+}_{0.7}Fe^{3+}_{1-x}Y^{3+}_{x}]O_4$, this is the cations distributions of yttrium-doped nickel–copper–cobalt ferrite. According to the characteristics of each cations, it is known that the four cations of nickel, copper, cobalt, and yttrium preferentially occupy the B positions of the octahedron, and the iron ions exist between the B positions of the octahedron and the A positions of the tetrahedron [29–31].

Combined with the Neel's molecular lattice model, the cation distributions in the ferrite doped with yttrium ions in nickel–copper–cobalt ferrite can be tentatively determined as the above formula, where Y_x indicates that a part of the iron ions at the B positions of the octahedron is replaced by Y^{3+} ions. According to the cation distributions of the yttrium-doped nickel–copper–cobalt ferrite, the average ionic radius (r) and oxygen parameter (u) of the B positions can be calculated from Eqs. (6) and (7) as shown in Table 3.

$$r_b = \frac{1}{2}\left[0.2r_{Ni^{2+}} + 0.1r_{Mg^{2+}} + 0.7r_{Co^{2+}} + (1-x)r_{Fe^{3+}} + xr_{Y^{3+}}\right] \tag{7}$$

$$u = \frac{5}{8} - \frac{(r_B + r_0)}{a} \tag{8}$$

where a is the lattice parameter and r_o is the oxygen ions radius (1.34 Å). We use the lattice parameter A and the experimental value of the oxygen parameter measured by XRD, and the distance between the cations and the cations and the distance between the cations and the anions can be calculated by the following formula. Specific data are shown

Table 2 Various structural parameters of $Ni_{0.2}Mg_{0.1}Co_{0.7}Fe_{2-x}Y_xO_4$ nanoferrite particles

Composition, x	Molecular weight 'M' (g/mol)	X-ray density 'ρ_x' (kg/m³)	Bulk density 'ρ_b' (kg/m³)	Porosity 'P' (%)	Tetrahedral site 'd_A' (Å)	Octahedral site 'd_B' (Å)
0.00	231.12	5243.92	3285.2	35.39	3.6229	2.9581
0.02	231.78	5250.82	3194.5	33.51	3.6247	2.9596
0.04	232.45	5263.31	3387.6	30.83	3.6255	2.9602
0.06	233.10	5278.02	3421.2	31.14	3.6246	2.9595
0.08	233.77	5296.81	3485.6	32.88	3.6245	2.9593

Table 3 Distance between cation–anion (Me–O) and cation–cation (Me–Me)

Content, x	Me–O (nm)				Me–Me (nm)					rB (nm)	U (nm)
	p	q	r	s	b	c	d	e	f		
0.00	0.0981	0.3734	0.7151	0.4264	0.4226	0.3524	0.3469	0.5434	0.5124	0.0687	0.3827
0.02	0.0983	0.3735	0.7152	0.4082	0.4223	0.3524	0.3470	0.5437	0.5126	0.0689	0.3826
0.04	0.0985	0.3731	0.7145	0.4080	0.4222	0.3523	0.3471	0.5438	0.5127	0.0692	0.3823
0.06	0.0986	0.3725	0.7132	0.4067	0.4224	0.3522	0.3470	0.5436	0.5126	0.0695	0.3819
0.08	0.0991	0.3720	0.7124	0.4066	0.4224	0.3520	0.3470	0.5436	0.5126	0.0697	0.3816
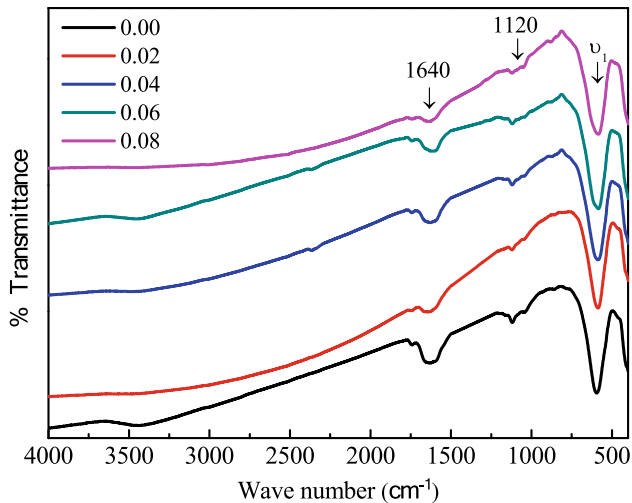
Fig. 4 FTIR spectra of $Ni_{0.2}Mg_{0.1}Co_{0.7}Fe_{2-x}Y_xO_4$ ($x = 0.0, 0.02, 0.04, 0.06, 0.08$) ferrite system

in Table 3, where b, c, d, e, and f are the distances between the cations and the cations, where p, q, r, and s, are the distances between the cations and the cations. The above data are calculated by these formulas [32]:

$$p = a\left(\frac{1}{2} - u\right) \quad q = \sqrt{3}a\left(u - \frac{1}{8}\right) \quad r = \sqrt{11}a\left(u - \frac{1}{8}\right)$$

$$s = \frac{\sqrt{3}}{3}a\left(u + \frac{1}{2}\right) \tag{9}$$

$$b = \frac{\sqrt{2}}{4}a \quad c = \frac{\sqrt{11}}{8}a \quad d = \frac{\sqrt{3}}{4}a \quad e = \frac{3\sqrt{3}}{8}a \quad f = \frac{\sqrt{6}}{4}a \tag{10}$$

3.3 Fourier infrared spectroscopy (FTIR)

Figure 4 is the Fourier infrared absorptions spectrum of all samples. In this figure, we can find that there is a distinct absorptions band of v_1 (see Table 4 for peak value), which is caused by vibrations between the metal atom and the oxygen atom, where v_1 is caused by the chemical bond vibrations between the metal ions and the oxygen ions at the B site of the octahedron [33]. v_2 is caused by the chemical bond

Table 4 Frequency bands v_1 of the samples

Composition, x	Sample	v_1 (cm^{-1})
0.00	$Ni_{0.2}Mg_{0.1}Co_{0.7}Fe_2O_4$	594
0.02	$Ni_{0.2}Mg_{0.1}Co_{0.7}Fe_{1.98}Y_{0.02}O_4$	586
0.04	$Ni_{0.2}Mg_{0.1}Co_{0.7}Fe_{1.96}Y_{0.04}O_4$	585
0.06	$Ni_{0.2}Mg_{0.1}Co_{0.7}Fe_{1.94}Y_{0.06}O_4$	584
0.08	$Ni_{0.2}Mg_{0.1}Co_{0.7}Fe_{1.92}Y_{0.8}O_4$	583

vibrations between the metal ions and the oxygen ions at the A site of the tetrahedron, which is not shown in the figure because it is beyond the measuring range of the instrument. It also proved that the sample is a spinel cube structure. In addition, we found that the other two smaller absorption bands are located at 1640 cm^{-1} and 1120 cm^{-1}. The absorption peak at 1640 cm^{-1} is caused by the vibrations of the H–O bond in the sample. The absorption peak at 1120 cm^{-1} is caused by the chemical vibrations of the C–O bond [34]. In Table 3, it can be observed that the positions of the octahedral absorptions peak have a certain relationship with the doping amount of Y^{3+}. The difference in the absorptions peak positions of v_1 and v_2 is mainly due to the difference in the bond length of Fe–O at the A and B sites, and the size of the bond length is related to the bond strength and the mass of the ions. Since the mass of Y (89 g/mol) is larger than the atomic mass of Fe (56 g/mol), when the Fe^{3+} at the B positions of the octahedron is replaced by Y^{3+}, the total mass of the B site will increase, causing the octahedral absorptions peak vibrations slowing down and causing a red shift.

3.4 Optical analysis (UV–Vis)

The optical bandgap (E_g) has formed an important property for the magnetoceramic Ni–Mg–Co ferrite with semiconductor properties. It has been used in many photoelectric devices. To study optical bandgap of these ferrites, the optical performance of the samples in the wave length range 230−850 nm is analyzed by UV–Vis absorptions spectra. In addition, the curves of the absorptions coefficient vs wavelength of the $Ni_{0.2}Mg_{0.1}Co_{0.7}Fe_{2-x}Y_xO_4$ ($x = 0.0, 0.02, 0.04, 0.06$ and 0.08) nanoferrites are shown
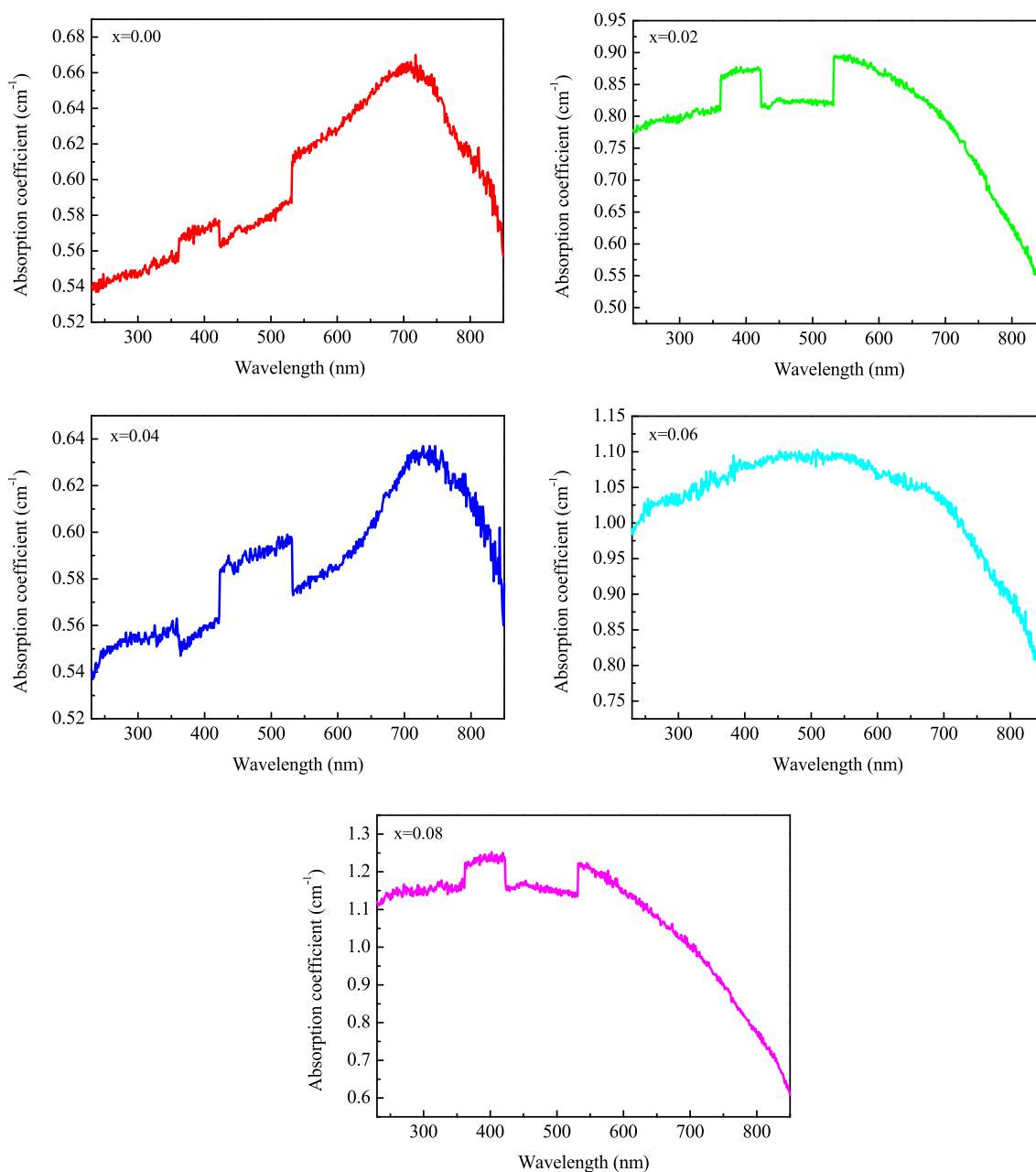
Fig. 5 UV–Vis absorbance spectra coefficient vs wavelength for $Ni_{0.2}Mg_{0.1}Co_{0.7}Fe_{2-x}Y_xO_4$ ($x=0.00$, 0.02, 0.04, 0.06 and 0.08) nanoferrites

in Fig. 5. The bandgaps here are associated with charge transfer between the cations at the tetrahedral and octahedral sites. It can be seen that there are different slopes at different wavelengths, which can be attributed to different electronic transitions between oxygen ions and cations. As can be seen from Fig. 5, the absorption intensity tends to increase with the increase of wavelength in the initial stage. In the last stage, the absorption intensity decreases rapidly with the increase of wavelength. It is noted that

these sharp absorptions bands are caused by various band defects introduced by doping other transitions metals [35].

The UV–Vis absorbance data were employed to construct the Tauc plot of the prepared $Ni_{0.2}Mg_{0.1}Co_{0.7}Fe_{2-x}Y_xO_4$ ($x=0.0$, 0.02, 0.04, 0.06 and 0.08) samples; a famous relations given by Tauc is used as given in Eqs. (11):

$$(\alpha h\nu)^{\frac{1}{n}} = A\left(h\nu - E_g\right) \tag{11}$$

where 'α' = adsorptions coefficient, 'h' = Planck's constant, 'ν' = frequency of light, 'E_g' = bandgap energy, 'A' = absorbance, and "n" is characteristic constant and related to type of electronic transitions. When "n" is 1/2, there would be direct transitions and 2 then it would be indirect electronic transitions. Figure 6 reflects the Tauc plots of all the $Ni_{0.2}Mg_{0.1}Co_{0.7}Fe_{2-x}Y_xO_4$ (x = 0.00, 0.02, 0.04, 0.06, and 0.08) nanoferrite samples. It is found that the optical bandgap of pure samples is 2.26 eV, while that of Y^{3+} ion-doped samples is 2.15 eV (x = 0.02), 2.09 eV (x = 0.04), 2.13 eV

(x = 0.06), and 2.16 eV (x = 0.08), respectively. This is also indirectly confirmed that the ferrite has semiconductor properties. The bandgap value gradually decreased from 2.26 eV to 2.09 eV with the increase of Y^{3+} ion doping content in Ni–Mg–Co ferrite, and the bandgap value gradually increased from 2.09 eV to 2.16 eV with the further increase of Y^{3+} io content. But, the optical bandgap of Ni–Mg–Co spinel ferrite decreases after doping rare earth Y^{3+} ions compared to pure sample. The highest bandgap value was found for the un-doped Ni–Mg–Co ferrite due to the orbital
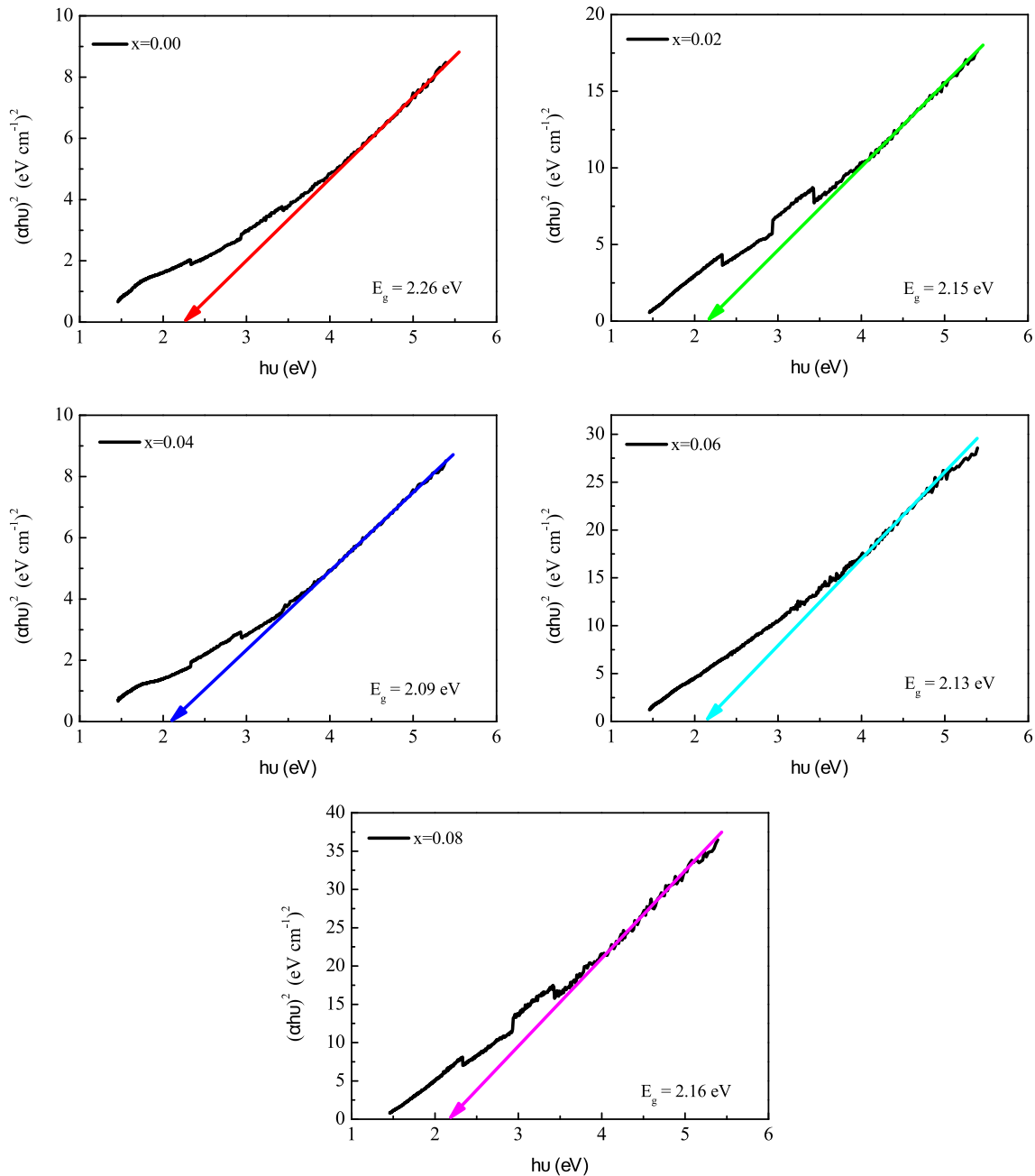

Fig. 6 Tauc plots for $Ni_{0.2}Mg_{0.1}Co_{0.7}Fe_{2-x}Y_xO_4$ (x = 0.00, 0.02, 0.04, 0.06, and 0.08) nanoferrites

overlap within the Fe–3d and O^{2-} p energy states [36]. However, with the doping of Y^{3+} ions, the bandgap value will decrease, because the defect energy (substituted point defect energy of Y_{Fe}) state of Y^{3+} ions will be generated near the conduction band. Therefore, the energy state of the defect interacts with the valence O^{2-} p orbital, which leads to the charge transfer from the defect energy state of Y^{3+} ions to the conduction band of Ni–Mg–Co ferrite.

3.5 Scanning electron microscopy (SEM)

Figure 7 is a photograph of a sample topography taken by a scanning electron microscope and a particle size distributions diagram of each sample. From the SEM photograph of the product, it is known that the nickel–magnesium–cobalt ferrite particles having different yttrium contents have small particle sizes, good dispersibility, and uniform size. Due to
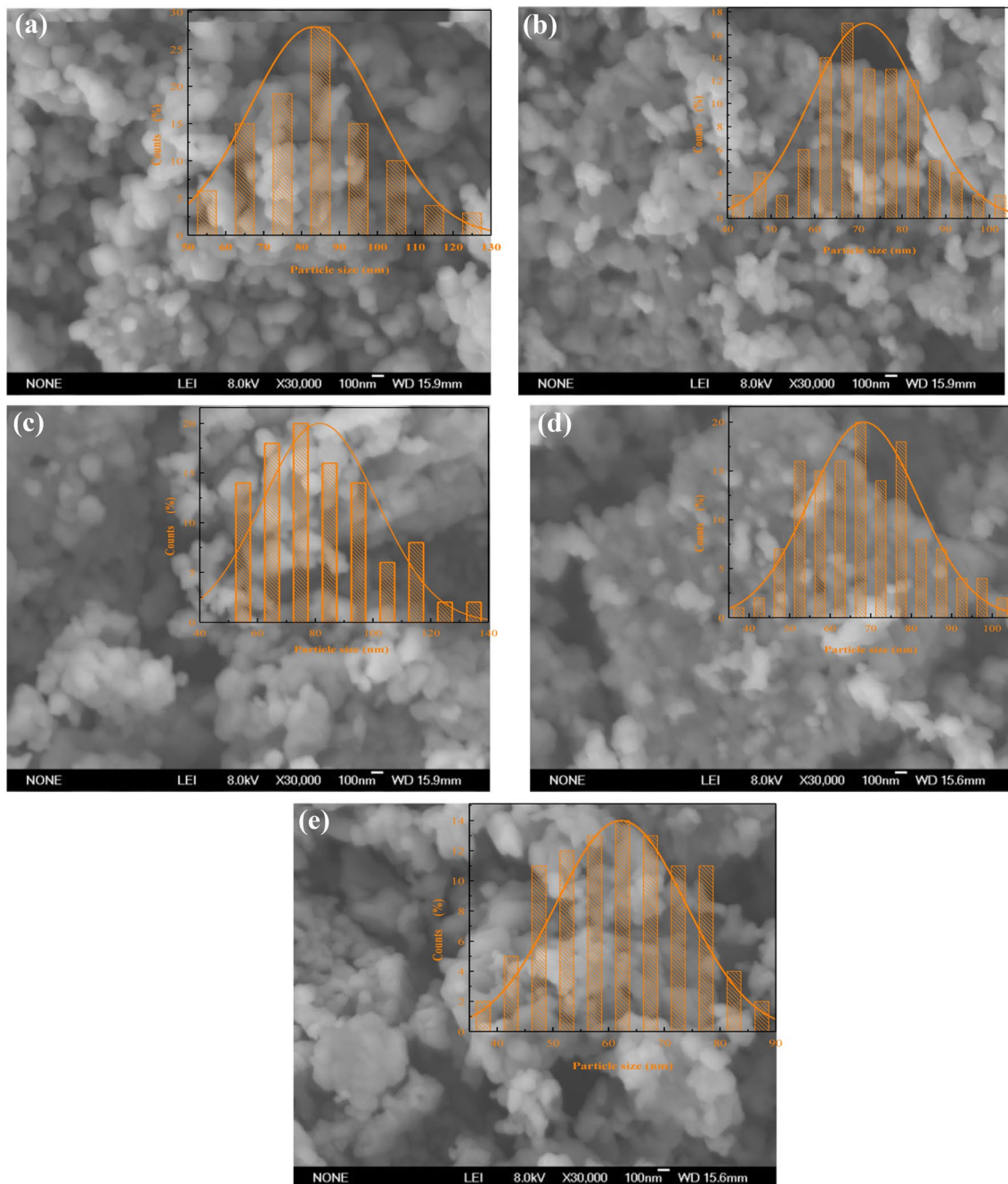

Fig. 7 Scanning electron microscopy micrographs of $Ni_{0.2}Mg_{0.1}Co_{0.7}Fe_{2-x}Y_xO_4$ ferrite nanoparticles: **a** $x=0.00$, **b** $x=0.02$, **c** $x=0.04$, **d** $x=0.06$, **e** $x=0.08$

the strong magnetic properties of the sample. The phenomenon of particle agglomerations is serious. However, the basic morphology of the sample particles can still be clearly seen. The sample particles are round or elliptical with a particle diameter of about 50 nm, which is basically consistent with the XRD test results. From the particle size distributions diagram, the product particle size distributions is narrow, both between 50 and 60 nm. It can also be seen in the figure that as the yttrium ions enter, the average size of the grains gradually decreases. It can be seen from the grain distribution diagram that the grain distributions present Gauss distributions. This shows that the particle size distributions of the sample is more uniform and the dispersions is better.

3.6 Elemental analysis

Five samples were tested using EDS and the results are shown in Fig. 8. In the test chart, we can clearly see that the five samples produced contain nickel, magnesium, cobalt, and oxygen chemical element. Four of the five samples have yttrium elements. In addition, the sample for elemental analysis is a certain area, so we can perform quantitative analysis based on the measured chemical element content. We can see that the chemical compositions ratio of the prepared sample is similar to the chemical compositions ratio of the target product. This finding gives us strong evidence that the preparations of the sample is the target product.

3.7 Magnetic research

The magnetic properties of ferrite materials are mainly derived from the magnetic properties of atoms. The magnetic properties of atoms come from the magnetic moment of electrons, but the movement of electrons is the source of the electronic magnetic moment. Therefore, adding a small amount of metal cations to a material inevitably changes the rotations state of the electrons in the atom and causes some changes in the magnetic properties of the material.

For spinel ferrite, its magnetic properties size mainly depends on the number of magnetic atoms in the crystal, the atomic magnetic moment, the superexchange interactions, and the external temperature. For the spinel-structured ferrite we prepared, the change of saturations magnetizations may be due to the following two points: (1) the magnetic moments of the A and B bits are arranged in opposite directions, so the total magnetic moment in the lattice is the net magnetic moment that the A and B bits not completely neutralize. Since the effective magnetic moment of Y^{3+} (close to 0 μ_B) is much smaller than that of Fe^{3+} (approximately 5 μ_B), as Y^{3+} replaces part of Fe^{3+}, the total magnetic moment of B bit decreases. The net magnetic moment decreases, causing the saturations magnetizations to decrease. (2) With the incorporations of Y^{3+}, it affects the superexchange

interactions in the crystal lattice. The superexchange interactions in spinel-structured ferrites are mainly A–B type and B–B type. One reason, the distance between two ions, among which the distance between metal ions and oxygen ions is the main one, the distance between metal ions also has an influence. The number of electrons in the outermost layer of metal ions and the orbital structure of their electron movement.

Such as nickel–magnesium–cobalt ferrite, the microstructure of this ferrite is a spinel structure. Adding a small amount of yttrium ions to this ferrite does change the microstructure of the ferrite. This is confirmed by X-ray diffractions and Fourier infrared. So there are some changes in the magnetic properties of matter. The unit cell of the spinel structure is shown in Fig. 9. One cell in the figure can be divided into eight small cubes, and the eight small cubes are further divided into two types, four for each type. The distribution of ions in the two small cubes is given in Fig. 8, respectively. The metal ion radius is smaller than the oxygen ion radius, so it is embedded in the gap between the oxygen ions. The gap is divided into two categories; one is an octahedral gap with a large gap (abbreviated as B positions) and the other is a tetrahedral gap with a small gap (referred to as A positions) (Fig. 9).

We used VSM to characterize the prepared samples, and the resulting hysteresis loop is shown in Fig. 10. The hysteresis loop can be used to read the saturation magnetizations M_s, remanent magnetizations M_r, coercive force, H_c of each sample and fill it into Table 6. The parameters related to the magnetic properties of the sample were calculated using the following formulas in conjunctions with the data in Table 6 and filled in Tables 5 and 6. The formula is as follows [37]:

$$\mu_{B(Cal.)} = M_B - M_A \qquad (12)$$

where 'μ_B' is the total magnetic moment 'M_A', 'M_B' is the magnetic moment of the metal ions at the A and B positions, respectively [38].

$$\mu_{B(exp.)} = \frac{M_W \times M_S}{5585} \qquad (13)$$

Among them are Bohr magnetons, 'M_w' is the molecular mass of the corresponding ferrites, and 'M_s' is the saturations magnetizations of the corresponding sample.

$$H_C = \frac{2K}{\mu_0 \times M_S} \qquad (14)$$

The saturations magnetizations 'M_s', coercive force 'H_c', and 'K' are magnetic anisotropy constants.

Figure 11a, b is based on the data in the table. It can be clearly seen in the figure that the magnetic parameters change with the amount of yttrium ions doped. The residual
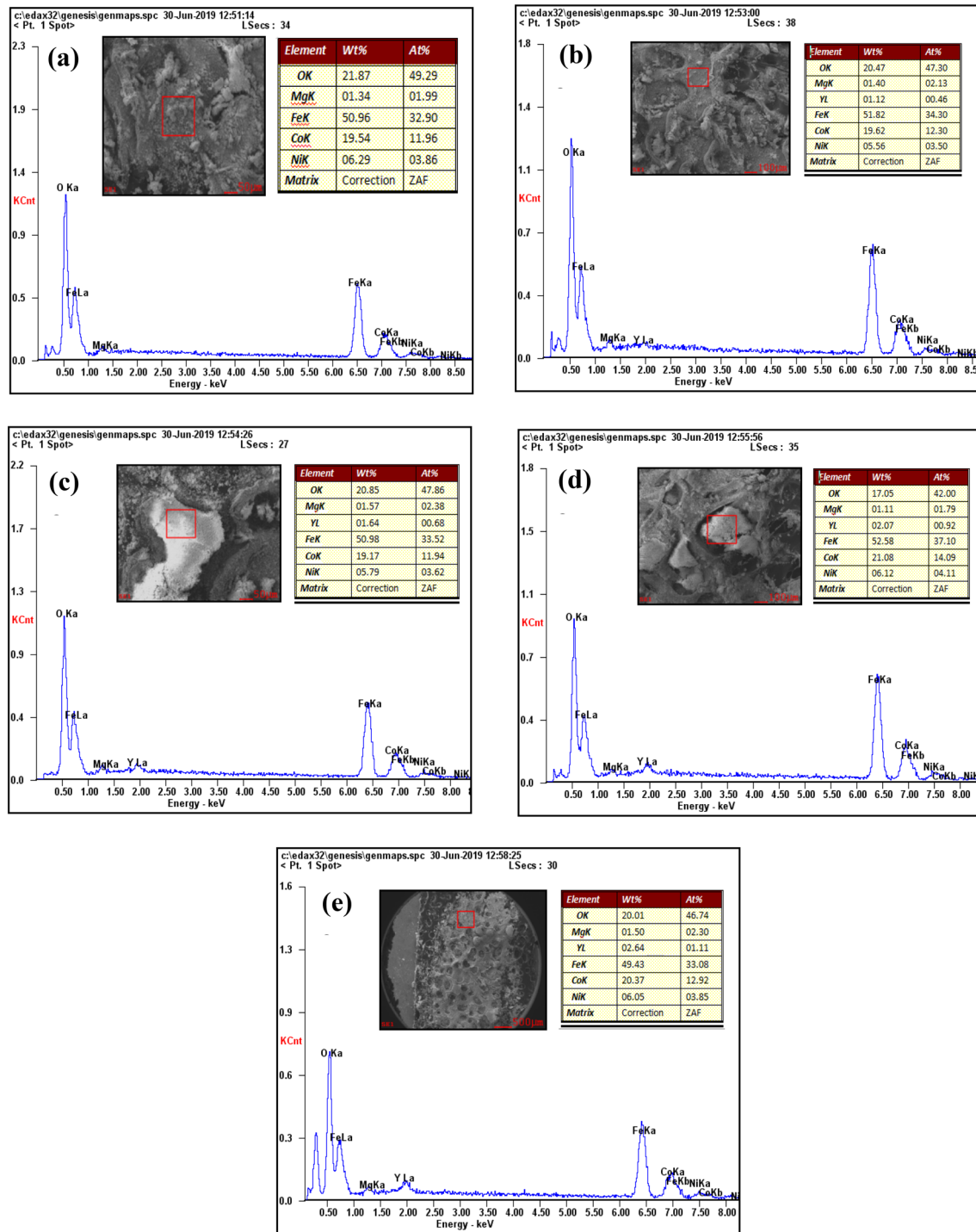
Fig. 8 EDS spectra of $Ni_{0.2}Mg_{0.1}Co_{0.7}Fe_{2-x}Y_xO_4$ ferrite nanoparticles: **a** $x=0.0$, **b** $x=0.02$, **c** $x=0.04$, **d** $x=0.06$, **e** $x=0.08$

magnetizations increased from 28.12 emu/g to 31.09 emu/g. This may be due to the fact that the anisotropy of the material in the polycrystal is small, but there is a strong stress, so the residual magnetization orientations in the material will be completely controlled by the stress. Under the actions of stress, the easy magnetizations axis determined by the

stress anisotropy belongs to the uniaxial anisotropy. At this time, the distribution of stress becomes uniform, and the residual magnetization increases. However, impurities may be generated as the amount of yttrium ions is increased. Because of the presence of impurities, a certain demagnetizing field is generated around the impurities and the pores,

Fig. 9 Ferrites crystallize in the form of a cubic structure. Each corner of a ferrite unit cell consists of a ferrite molecule. **a** Tetrahedral or A sites, **b** octahedral or B sites
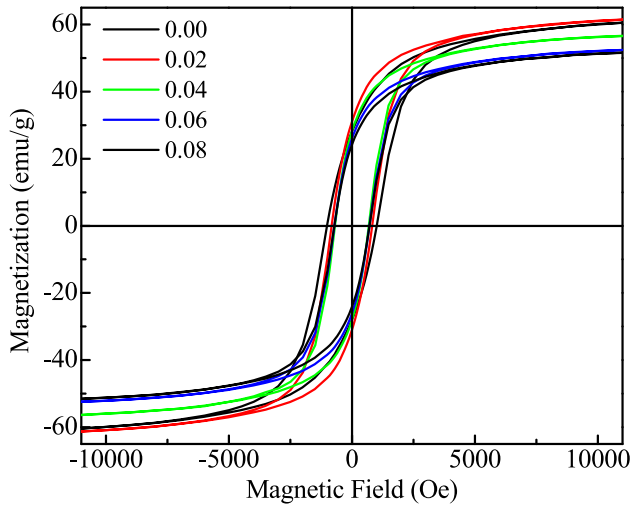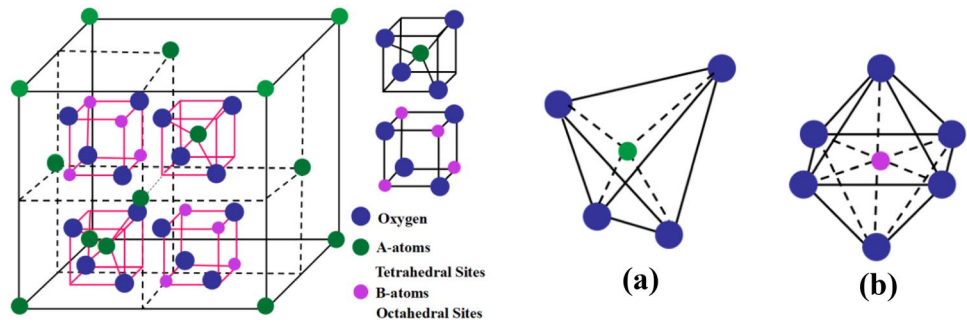

Fig. 10 M–H hysteresis loops of $Ni_{0.2}Mg_{0.1}Co_{0.7}Fe_{2-x}Y_xO_4$ ($x=0.00$, 0.02, 0.04, 0.06, 0.08) ferrite system

rectangular ratio of the hysteresis loop is reduced, so that the residual magnetization reduction is reduced to 25.54 emu/g.

Generally, the coercive force H_c is inversely proportional to the saturations magnetizations M_s and is proportional to the magnetocrystalline anisotropy constant K and the internal stress. The coercive force H_c is related to the microstructure of the magnetic material in addition to the intrinsic properties of the magnetic material. Generally, the grain size of the magnetic substance is very large, the grain boundary is thick, the uniformity is poor, and the coercive force is larger when the pores are dispersed in the grain boundary and the grain boundary. In the sample prepared this time, the saturation magnetization increases first and then decreases, the anisotropy constant decreases, and the internal stress does not decrease, so the coercivity of the material decreases. In addition, the size of the crystal grains is an important factor affecting the magnitude of the coercive force. When the grain size of the spinel nickel–magnesium–cobalt ferrite nanoparticles is smaller than the critical dimensions of the magnetic single domains, the coercive force becomes low. In summary, the coercivity of the sample is affected by many factors leading to a decrease in coercivity.

The hysteresis loop is subjected to differential processing to obtain a curve as shown in Fig. 10, and the data are analyzed to obtain magnetic susceptibility and filled in
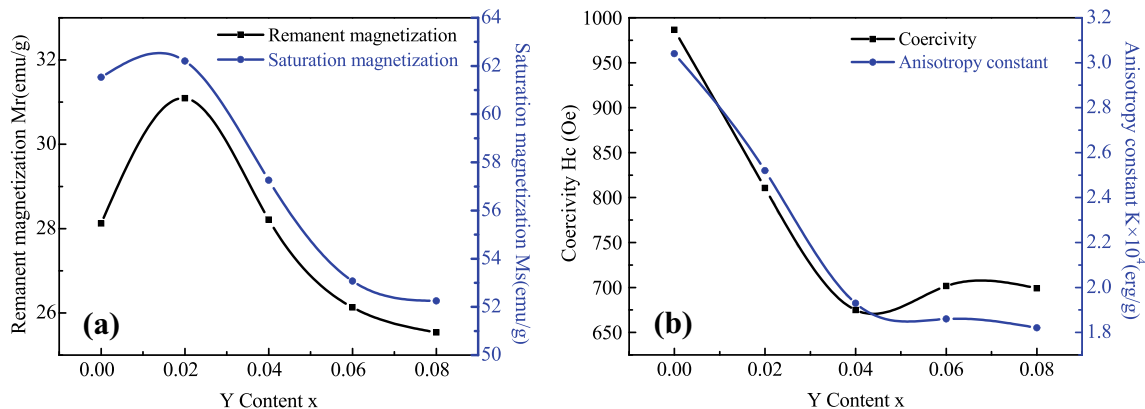
so that the magnetization inside the material is not uniform, so that the residual magnetization becomes low. In the process of demagnetizations, the growth of demagnetized nuclei may be due to the inhomogeneity of impurity pore. The

Fig. 11 Variation of saturation magnetization, remanent magnetization, anisotropy constant, and coercivity with Y^{3+} content

Table 5 Magnetic parameters of the prepared ferrite samples

Composition, x	Remanent magnetization, M_r (emu/g)	Saturation magnetization, M_s (emu/g)	Coercivity, H_c (Oe)	Squareness, S (M_r/M_s)	Switching field distribution SFD (dH/H_c)
0.00	28.12	61.53	986.55	0.508	0.80
0.02	31.09	62.20	810.59	0.607	0.93
0.04	28.21	57.26	674.92	0.595	0.92
0.06	26.13	53.07	701.68	0.577	0.89
0.08	25.54	52.25	698.99	0.597	0.98

Table 6 The values of magnetic moment, magnetic anisotropy, dM/dH, and H_m calculated from $M(H)$ data for $Ni_{0.2}Mg_{0.1}Co_{0.7}Fe_{2-x}Y_xO_4$ ($x=0.00, 0.02, 0.04, 0.06, 0.08$)

Composition, x	Unit cell mag. mom, $\mu_{B(exp.)}$	Anisotropy constant $K \times 10^4$ (erg/g)	H_m (Oe)	dM/dH (emu/(g Oe))$\times 10^{-3}$	
				$H \rightarrow 0$	$H \rightarrow H_m$
0.00	2.55	3.04	997	17.73	41.36
0.02	2.58	2.52	898	22.75	56.34
0.04	2.38	1.93	689	23.31	59.93
0.06	2.21	1.86	798	21.08	52.80
0.08	2.20	1.82	798	19.83	48.94

Fig. 12 Configuration of ion pairs in spinel ferrites with favorable distances

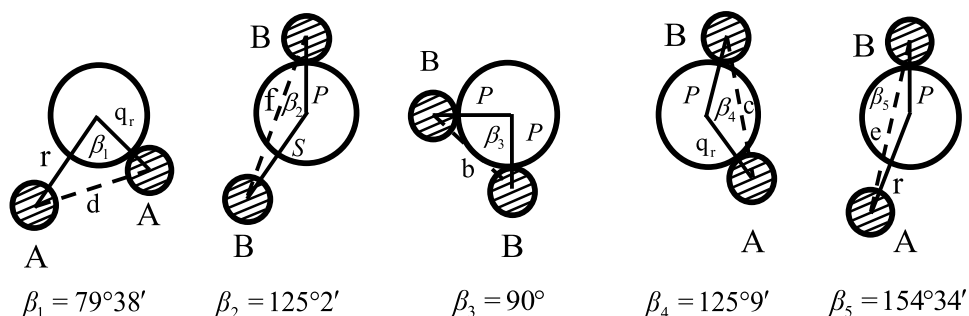$\beta_1 = 79°38'$ $\beta_2 = 125°2'$ $\beta_3 = 90°$ $\beta_4 = 125°9'$ $\beta_5 = 154°34'$

Table 6. The parameters in Tables 5 and 6 were analyzed to determine the saturations magnetizations of the sample, and the residual magnetization was varied with the amount of yttrium ions incorporated. When $x = 0.02$, the parameters of the sample reached a maximum; therefore, it can be concluded that the sample has the best magnetic properties when $x = 0.02$. The coercivity and the anisotropy constants show a downward trend, and the trend of change can be clearly seen in Figs. 9a and b. The saturation magnetization increased from 61.53 to 62.20 emu/g and then decreased to 52.2 emu/g. Mainly due to the incorporations of yttrium ions into the octahedral gap (B positions), resulting in some of the original ferric ions in the octahedral gap entering the tetrahedral gap (A positions). According to the Neel theory, the Superexchange between A and B in the crystal plays a leading role, and the entry of yttrium ions increases the Superexchange effect, resulting in an increase in saturations magnetizations. When the doping is further increased, the interactions between the yttrium ions and the iron ions in the octahedron increases, destroying the original motions state of the electrons outside the two ions [39]. The ordering of the magnetic moments affecting the iron ions leads to a decrease in the net magnetic moment and a decrease in the saturation magnetization [40]. The type of superexchange [41] effect is shown in Fig. 12.

According to the data of Fig. 13, it is filled in Table 6, from which it can be seen that the value of the magnetic susceptibility when H reaches the maximum values is 41.36, 56.34, 59.93, 52.80, and 48.94 emu/(g Oe))$\times 10^{-3}$. When H approaches 0, the magnetic susceptibility values are (17.73, 22.75, 23.31, 21.08, and 19.83 emu/(g Oe))$\times 10^{-3}$. Maximum coercivity (997, 898, 689, 798, and 798 Oe). In Fig. 13, it is also observed that the peak
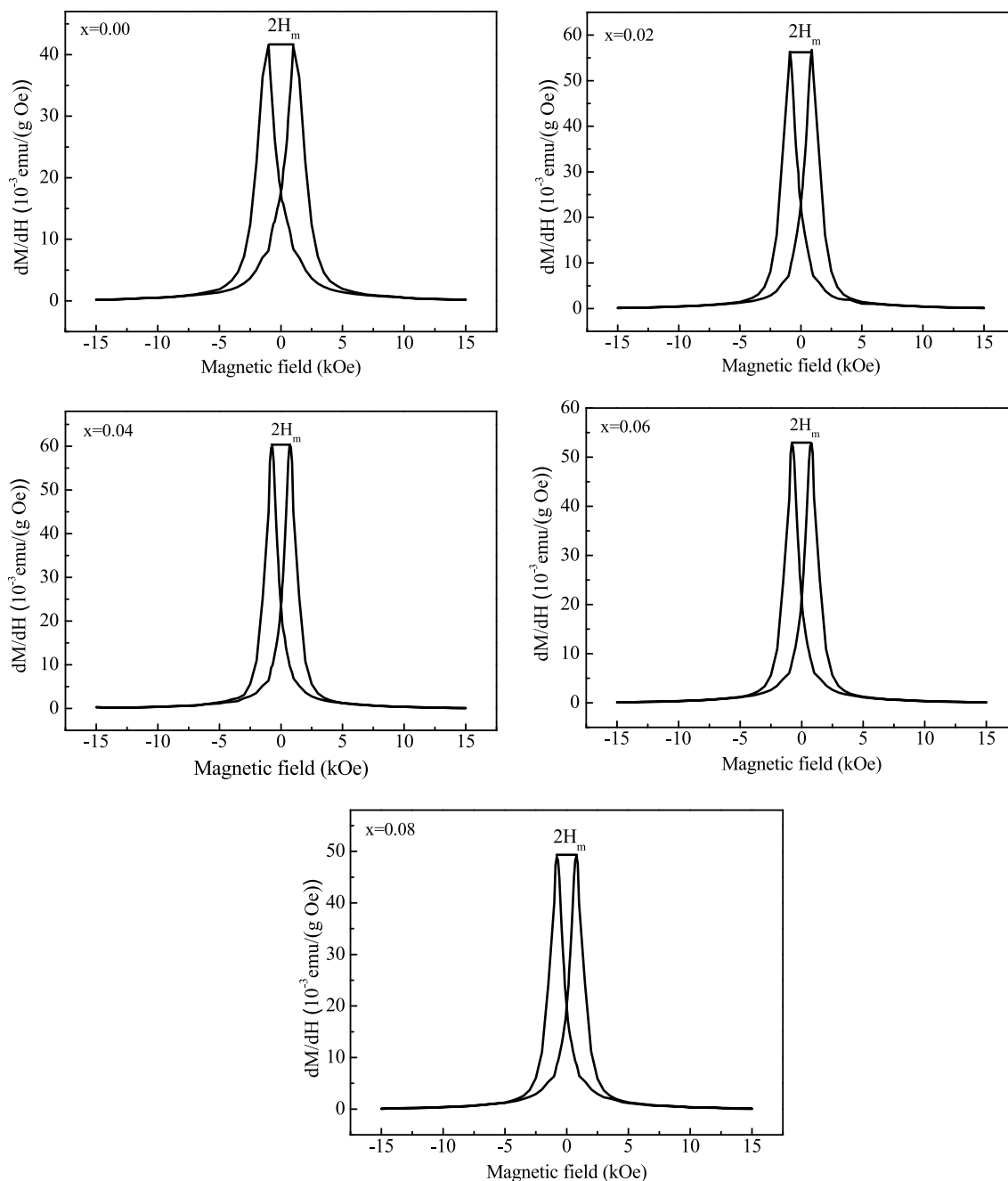
Fig. 13 Field dependence of dM/dH of different samples. $2H_m$ measures the magnetic field that separates two peaks

height of the magnetic susceptibility decreases when the coercive force takes the maximum value, and the separation between the peaks indicates that the grain size is large, and the sample with a good cubic spinel structure is in a magnetically unstable. This also indicates that the nickel–magnesium–cobalt ferrite doped with yttrium ions is a low-magnetic multi-iron material.

4 Conclusions

The prepared samples were characterized using XRD, FTIR, UV–Vis, SEM, EDS, and VSM. XRD indicates that the prepared sample is a pure cubic spinel structure and has good crystallinity. This means doping with a proper amount of Y^{3+} does not change the spinel structure of the ferrite. However, the entry of yttrium ions into the crystal lattice will

cause a slight change in the crystal plane spacing and grain size of the sample. FTIR also confirmed that the prepared samples contained chemical functional groups such as Fe–O and C–O. These two characterizations proved that yttrium ions were successfully doped into Ni–Mg–Co ferrite system and the micro-doping of ions can change the microstructure of the sample. It can be seen from the characterization results of the UV–Vis spectrum of the sample that the slight doping of ions can change the optical bandgap of the ferrite sample. In the SEM image, can clearly see that each particle of the sample has an elliptical particle shape and a relatively uniform distributions, but the sample particles are agglomerated due to strong magnetic properties, so that there are large particles. EDS characterization shows that the sample contains chemical elements such as nickel, magnesium, and cobalt. In addition, it can be seen that the proportion of chemical elements in the prepared sample is similar to the target product.

The VSM test results indicate the saturation magnetizations of the sample and the residual magnetizations increases first and then decreases with the increase of the amount of yttrium ions. For high-density magnetic recording medium materials, we generally require smaller SFD and bigger squareness. Compared with pure sample and other doped samples, the switching field distributions (SFD) and the squareness (M_r/M_s) are the best when the doping amount $x = 0.02$. So it can be concluded that the sample has the best magnetic properties, more suitable for magnetic recording materials.

Compliance with ethical standards

References

1. L. Bozadgiev, T. Dimova, T. Mitev, Classifications of ferrospinel structures and textures. J. Am. Ceram. Soc. (1985). https://doi.org/10.1111/j.1151-2916.1985.tb15250.x
2. M. Rostami, M. Rahimi-Nasrabadi, M.R. Ganjali et al., Facile synthesis and characterizations of TiO_2–graphene–$ZnFe_{2-x}Tb_xO_4$ ternary nano-hybrids. J. Mater. Sci. **52**, 7008–7016 (2017)
3. B. Geller, A. Coville, Magnetism and magnetic materials. Phys. Today **11**, 48–48 (1958)
4. A.T. Raghavendar, D. Pajic, K. Zadro, T. Milekovic, P.V. Rao, K.M. Jadhav, D. Ravinder, J. Magn. Magn. Mater. **316**, 1–7 (2007)
5. C. Venkataraju, G. Sathishkumar, K. Sivakumar, J. Magn. Magn. Mater. **323**, 1817–1822 (2011)
6. L. Zhao, H. Yang, L. Yu, Y. Cui, X. Zhao, B. Zou, S. Feng, J. Magn. Magn. Mater. **301**, 445–451 (2006)
7. S. Uday Bhasker et al., Preparations and characterizations of cobalt magnesium nano ferrites using auto-combustions method. Adv. Mater. Res. **584**, 280–284 (2012)
8. N. Ranvah, Y. Melikhov, I.C. Nlebedim, D.C. Jiles, J.E. Snyder, A.J. Moses, P.I. Williams, Temperature dependence of magnetic anisotropy of germanium/cobalt cosubstituted cobalt ferrite. J. Appl. Phys. **105**, 5181–5183 (2009)
9. S.U. Bhasker, Reddy MR Effect of chromium substitutions on structural, magnetic and electrical properties of magneto ceramic cobalt ferrite nano-particles. J. Sol-Gel Sci. Technol. **73**, 396–402 (2015)
10. J.A. Paulsen, C.C.H. Lo, J.E. Snyder, A.P. Ring, L.L. Jones, D.C. Jiles, Study of the curie temperature of cobalt ferrite based composites for stress sensor applications. IEEE. Trans. Magn. **39**, 3316–3318 (2003)
11. K.K. Bharathi, J.A. Chelvane, Markandeyulu G Magneto electric properties of Gd and Nd-doped nickel ferrite. J. Magn. Magn. Mater. **321**, 3677–3680 (2009)
12. M. R ahimi-Nasrabadi, M. Behpour, A. Sobhani-Nasab, S. MostafaHosseinpour-Mashkani, $ZnFe_{2-x}La_xO_4$ nanostructure: synthesis, characterizations, and its magnetic properties. J. Mater. Sci. Mater. Electron. **26**, 9776–9781 (2015)
13. M. Rahimi-Nasrabadi, M. Behpour, A. Sobhani-Nasab, Nanocrystalline Ce-doped copper ferrite: synthesis, characterizations, and its photocatalyst applications. J. Mater. Sci. Mater. Electron. **27**, 11691–11697 (2016)
14. M. Rahimi-Nasrabadi, M. Rostami, F. Ahmadi, Synthesis and characterizations of $ZnFe_{(2-x)}Yb_xO_{4-x}$graphene nanocomposites by sol–gel method. J. Mater. Sci. Mater. Electron. **27**, 11940–11945 (2016)
15. S.M. Peymani-Motlagh, N. Moeinian, M. Rostami et al., Effect of Gd^{3+}-, Pr^{3+}- or Sm^{3+}-substituted cobalt–zinc ferrite on photodegradations of methyl orange and cytotoxicity tests. J. Rare Earths **37**, 1288–1295 (2019)
16. X. Pan, A. Sun, Y. Han, Structural and magnetic properties of Bi3+ ions doped Ni–Cu–Co nano ferrites prepared by sol–gel auto combustions method. J. Mater. Sci. Mater. Electron. **30**, 4644–4657 (2019)
17. K. Chen, H. Yang, F. Liang et al., Microwave-irradiations-assisted combustions toward modified graphite as lithium ions battery anode. ACS Appl. Mater. Interfaces **10**, 909–914 (2017)
18. K. Chen, H. Yang, F. Liang, D. Xue, A.C.S. Appl, Mater. Interfaces **10**, 909–914 (2018)
19. A. Gholizadeh, E. Jafari, Effects of sintering atmosphere and temperature on structural and magnetic properties of Ni–Cu–Zn ferrite nano-particles: Magnetic enhancement by a reducing atmosphere. J. Magn. Magn. Mater. **422**, 328–336 (2017)
20. Z. Liu, Z. Peng, C. Lv et al., Doping effect of Sm^{3+} on magnetic and dielectric properties of Ni–Zn ferrites. Ceram. Int. **43**, 1449–1454 (2017)
21. U. Kurtan, R. Topkaya, S. Esir, A. Baykal, Sol–gel auto combustions synthesis of CoFe2O4/1-methyl-2-pyrrolidone nanocomposite: its magnetic characterizations. Ceram. Int. **39**, 6407–6413 (2013)
22. M.A. Ahmed, S.F. Mansour, M. Afifi, Structural and electrical properties of nanometric Ni–Cu ferrites synthesized by citrate precursor method. J. Magn. Magn. Mater. **324**, 4–10 (2012)
23. B.R. Babu, M.S.R. Prasad et al., Structural and magnetic properties of $Ni_{0.5}Zn_{0.5}Al_xFe_{2-x}O_4$ nano ferrite system. J. Mater. Chem. Phys. **148**, 585–591 (2014)
24. M. Kaiser, Effect of nickel substitutions on some properties of Cu–Zn ferrites. J. Alloys Compd. **468**, 15–21 (2009)
25. C. Sujatha, K.V. Reddy, K.S. Babu, A.R. Reddy, Rao KH Effect of sintering temperature on electromagnetic properties of NiCuZn ferrite. Ceram. Int. **39**, 3077–3086 (2013)

26. D. Cullity, S.R. Stock, Elements of X-ray diffractions: Pearson new international editions. Fuel **102**, 716–723 (2012)

27. K. Siraj, M. Khaleeq-ur-Rahman, S.I. Hussain, M.S. Rafique, S. Anjum, Effect of depositions temperature on structural, surface, optical and magnetic properties of pulsed laser deposited Al doped CdO thin films. J. Alloys Compd. **509**, 6756–6762 (2011)

28. V.J. Angadi, B. Rudraswamy, K. Sadhana, S.R. Murthy, K. Praveena, Effect of Sm^{3+}–Gd^{3+} on structural, electrical and magnetic properties of Mn–Zn ferrites synthesized via combustions route. J. Alloys Compd. **656**, 5–12 (2016)

29. K. Krieble, T. Schaeffer, J.A. Paulsen, A.P. Ring, C.C.H. Lo, J.E. Snyder, Mössbauer spectroscopy investigations of Mn-substituted Co-ferrite (Co $Mn_xFe_{2-x}O_4$). J. Appl. Phys. **97**, 98–101 (2005)

30. J.M. Hastzngs, L.M. Corliss, Neutron diffractions studies of zinc ferrite and nickel ferrite. Rev. Mod. Phys. **25**, 114–119 (1953)

31. G.A. Sawatzky, F.V.D. Woude, A.H. Morrish, Mossbauer study of several ferrimagnetic spinels. Phys. Rev. **187**, 747–757 (1969)

32. M.M. Eltabey, K.M. El-Shokrofy, S.A. Gharbia, Enhancement of the magnetic properties of Ni–Cu–Zn ferrites by the non-magnetic Al^{3+}-ions substitutions. J. Alloys Compd. **509**, 2473–2477 (2011)

33. M. Ashokkumar, $Zn_{0.96-x}Cu_{0.04}Fe_xO$ ($0 \leq x \leq 004$) alloys—optical and structural studies. Superlattices Microstruct. **69**, 53–64 (2014)

34. P.A. Shaikh, R.C. Kambale, A.V. Rao, Y.D. Kolekar, Effect of Ni doping on structural and magnetsic properties of $Co_{1-x}Ni_xFe_{1.9}Mn_{0.1}O_4$. J. Magn. Magn. Mater. **322**, 718–726 (2010)

35. M.W. Mushtaq et al., Synthesis, structural and biological studies of cobalt ferrite nanoparticles. Bulg. Chem. Commun. **48**, 3–565 (2015)

36. S. Patil, H.B. Naik, G. Nagaraju, R. Viswanath, S. Rashmi, Synthesis of visible light active Gd^{3+}-substituted $ZnFe_2O_4$ nanoparticles for photocatalytic and anti-bacterial activities. Eur. Phys. J. **132**, 320–328 (2017)

37. R.C. Kambale, P.A. Shaikh, S.S. Kamble, Y.D. Kolekar, Effect of cobalt substitutions on structural, magnetic and electric properties of nickel ferrite. J. Alloys Compd. **478**, 599–603 (2009)

38. D. Fritsch, C. Ederer, Epitaxial strain effects in the spinel ferrites $CoFe_2O_4$ and $NiFe_2O_4$ from first principles. Phys. Rev. B **82**, 104–117 (2010)

39. C.N. Chervin, B.J. Clapsaddle, H.W. Chiu et al., Role of cyclic ether and solvent in a non-alkoxide sol–gel synthesis of yttria-stabilized zirconia nanoparticles. Chem. Mater. **18**, 4865–4874 (2006)

40. V. Chaudhari, S.E. Shirsath, M.L. Mane, R.H. Kadam, S.B. Shelke, Mane DR Crystallographic, magnetic and electrical properties of $Ni_{0.5}Cu_{0.25}Zn_{0.25}La_xFe_{2-x}O_4$ nanoparticles fabricated by sol–gel method. J. Alloys Compd. **549**, 213–220 (2013)

41. I.P. Muthuselvam, R.N. Bhowmik, Mechanical alloyed Ho~$(^{3+})$ doping in $CoFe_2O_4$ spinel ferrite and understanding of magnetic nanodomains. J. Magn. Magn. Mater. **322**, 767–776 (2010)